Journal of the Mechanics and Physics of Solids 63 (2014) 62–79

Contents lists available at ScienceDirect

Journal of the Mechanics and Physics of Solids

journal homepage: www.elsevier.com/locate/jmps

Effect of inclusion density on ductile fracture toughness and roughness

A. Srivastava [a], L. Ponson [b], S. Osovski [a], E. Bouchaud [c], V. Tvergaard [d], A. Needleman [a,*]

[a] Department of Materials Science & Engineering, University of North Texas, Denton, TX, USA
[b] Institut Jean le Rond d'Alembert (UMR 7190), CNRS—Université Pierre et Marie Curie, Paris, France
[c] ESPCI, Paris Tech, Paris, France
[d] Department of Mechanical Engineering, The Technical University of Denmark, Lyngby, Denmark

ARTICLE INFO

Article history:
Received 22 July 2013
Received in revised form
28 September 2013
Accepted 6 October 2013
Available online 12 October 2013

Keywords:
Ductile fracture
Fracture toughness
Fracture surface roughness
Micromechanical modeling
Finite elements

ABSTRACT

Three dimensional calculations of ductile fracture under mode I plane strain, small scale yielding conditions are carried out using an elastic-viscoplastic constitutive relation for a progressively cavitating solid with two populations of void nucleating second phase particles. Larger inclusions that result in void nucleation at an early stage are modeled discretely while smaller particles that require large strains to nucleate voids are homogeneously distributed. Full field solutions are obtained for eight volume fractions, ranging from 1% to 19%, of randomly distributed larger inclusions. For each volume fraction calculations are carried out for seven random distributions of inclusion centers. Crack growth resistance curves and fracture surface roughness statistics are calculated using standard procedures. The crack growth resistance is characterized in terms of both J_{IC} and the tearing modulus T_R. For all volume fractions considered, the computed fracture surfaces are self-affine over a size range of nearly two orders of magnitude with a microstructure independent roughness exponent of 0.53 with a standard error of 0.0023. The cut-off length of the scale invariant regime is found to depend on the inclusion volume fraction. Consideration of the full statistics of the fracture surface roughness revealed other parameters that vary with inclusion volume fraction. For smaller values of the discretely modeled inclusion volume fraction ($\leq 7\%$), there is a linear correlation between several measures of fracture surface roughness and both J_{IC} and T_R. In this regime crack growth is dominated by a void-by-void process. For greater values of the discretely modeled inclusion volume fraction, crack growth mainly involves multiple void interactions and no such correlation is found.

1. Introduction

Two fundamental questions in the mechanics and physics of fracture are:

1. What is the relation between observable features of a material's microstructure and its resistance to crack growth?
2. What is the relation between observable features of a material's microstructure and the roughness of the fracture surface?

An obvious corollary question is: What is the relation, if any, between a material's crack growth resistance and the roughness of the corresponding fracture surface?

* Corresponding author. Tel.: +1 940 369 7715.
E-mail address: needle@unt.edu (A. Needleman).

0022-5096/$ - see front matter © 2013 Elsevier Ltd. All rights reserved.
http://dx.doi.org/10.1016/j.jmps.2013.10.003

Here, we report on calculations of ductile crack growth aimed at addressing these questions. At room temperature, ductile fracture of structural metals generally occurs by the nucleation, growth and coalescence of micron scale voids. The voids nucleate either by debonding or cracking of inclusions and/or second phase particles. This process was identified by Tippur (1949) and subsequently documented by Puttick (1959), Rogers (1960) and Gurland and Plateau (1963). Micromechanical modeling of this process of ductile fracture initiated with the work of McClintock (1968) and Rice and Tracey (1969). Reviews from a range of perspectives and with extensive references are available from Goods and Brown (1979), Garrison and Moody (1987), Tvergaard (1990) and Benzerga and Leblond (2010).

In a variety of structural alloys, the distribution of void nucleating particles can be idealized as involving two size scales; larger inclusions that nucleate voids at relatively small strains and smaller particles that nucleate voids at much larger strains. The size of the void nucleating particles is typically between 0.1 μm and 100 μm, with volume fractions of no more than a few percent. It is well appreciated that the distribution of void nucleating particles plays a major role in setting the crack growth resistance in such materials. We idealize such a microstructure by modeling the larger inclusions discretely (e.g. MnS inclusions in steels) to introduce a length scale, while the smaller particles (e.g. carbides in steels) are taken to be homogeneously distributed. This type of idealized microstructure has been used in a variety of 2D and 3D ductile fracture studies, e.g. Needleman and Tvergaard (1987), Mathur et al. (1996), Tvergaard and Needleman (2006). However, it is only recently that the computational capability has been available, e.g. Needleman et al. (2012), Tang et al. (2013), to compute ductile crack growth of sufficient extent and in sufficient detail to quantify fracture surface roughness as in Needleman et al. (2012), Ponson et al. (2013, submitted for publication).

Although the qualitative study of fracture surface morphology dates back to the sixteenth century, technological advancements (ASM Handbook, 1987) and advancements in the description of complex scale invariant geometries (Feder, 1988) in the twentieth century have made quantitative statistical fractography possible. In particular, Mandelbrot et al. (1984) were the first to quantitatively characterize the scale invariant properties of fracture surfaces and termed them fractal (Mandelbrot, 1983). Subsequently, the distinction between self-similar and self-affine objects was appreciated (Mandelbrot, 1985). A function $y=h(x)$ is said to exhibit self-similar (or fractal) properties if it remains statistically invariant under a uniform dilatation in the x and y directions, while a self-affine function is statistically invariant under the anisotropic scaling $h(\lambda x)=\lambda^H h(x)$. A self-affine function with Hurst exponent H is a fractal object with dimension $D=2-H$ (where D is the box or Minkowski–Bouligand dimension, see e.g. Moreira et al., 1994) when viewed at sufficiently small length scales but is an ordinary one dimensional object ($D=1$) when viewed over a sufficiently large length scale, see for example Barabasi and Stanley (1995) or Feder (1988). Fracture surfaces have been shown to be self-affine, not self-similar. The self-affine nature of the roughness of fracture surfaces can be characterized by the Hurst exponent of the correlation function of the fracture surface profile, also referred to as the roughness exponent. The self-affine nature of the roughness of fracture surfaces has been observed over a range of size scales in a wide variety of materials (metals, ceramics, glasses, rocks) and under a wide variety of loading conditions (quasi-static, dynamic, fatigue), see for example Underwood and Banerji (1986), Dauskardt et al. (1990), Cherepanov et al. (1995), Bouchaud (1997), Charkaluk et al. (1998).

In Mandelbrot et al. (1984) a negative correlation was found between what they termed the fractal dimension of the fracture surface roughness and the corresponding impact energy (equivalent to a positive correlation with the roughness exponent). This gave rise to the hope that the fractal dimension of the fracture surface roughness could be related to the material's toughness. Subsequent studies have been inconclusive, with some studies reporting a positive correlation, Wang et al. (1988), Ray and Mandal (1992), others a negative correlation, Mu and Lung (1988), Su et al. (1991), Carney and Mecholsky (2013) reported a positive or negative correlation depending on the fracture mechanism, and still others reported no correlation, Pande et al. (1987), Richards and Dempsey (1988), Davidson (1989). Charkaluk et al. (1998) argued that the discrepancy between these results is related to the methods used to calculate the fractal dimension.

Bouchaud et al. (1990) proposed that the exponent characterizing the scale invariance of the fracture surface roughness is universal, i.e. independent of the material and its toughness as long as the fracture mechanism remains fixed. Alternatively, a multifractal characterization of fracture surface roughness has been suggested as discussed at length by Cherepanov et al. (1995). Dauskardt et al. (1990) suggested that the scaling properties of the fracture surface may depend on the fracture mechanism and/or the range of length scales considered. Ponson et al. (2006) characterized the roughness scaling in terms of two exponents, one for the roughness in the direction of crack propagation and the other for the roughness parallel to the crack front. Bonamy et al. (2006) (see also Bonamy and Bouchaud, 2011) argued that there are two roughness regimes, one pertaining to length scales smaller than the fracture process zone and the other to length scales larger than the fracture process zone, with each regime characterized by different values of scaling exponents. More recently, Bouchbinder et al. (2006), Vernède et al. (submitted for publication), Ponson et al. (2013) have stressed the importance, particularly for ductile fracture, of considering the full fracture surface statistics, not just the correlation function. The full roughness statistics of the calculated ductile fracture surfaces in Ponson et al. (2013) were found to vary with the fracture parameters.

A variety of models have been introduced aimed at understanding and simulating the scaling characteristics of fracture surfaces, e.g. Ramanathan et al. (1997), Dauskardt et al. (1990), Bouchbinder et al. (2004), Afek et al. (2005), but these have only focused on the value of the roughness exponent and do not provide a basis for calculating crack growth resistance as well as roughness. Here, as in Needleman et al. (2012), Ponson et al. (2013, submitted for publication), we report on 3D finite deformation calculations of ductile crack growth under small scale yielding conditions with imposed monotonically increasing mode I remote loading. The analyses are based on a constitutive framework for a progressively cavitating ductile

solid stemming from the work of Gurson (1975). An advantage of such simulations, presuming that they are physically realistic, is that one feature of the microstructure can be varied with all other material characteristics fixed and the fracture process can be constrained to involve only one mechanism. This is difficult, if not impossible, to do in experiments.

In the calculations reported here, the material and fracture properties are fixed and only the volume fraction of, or equivalently the mean spacing between, the larger void nucleating inclusions is varied. Fracture toughness and fracture surface roughness results are reported for eight volume fractions, ranging from 1% to 19%, of fixed size inclusions. For each inclusion volume fraction seven realizations were analyzed. The results presented here extend those in Ponson et al. (submitted for publication). The crack growth resistance is quantified both in terms of J_{IC} (ASTM E1820-11, 2011) and the tearing modulus, T_R (Paris et al., 1979). Quantities characterizing the fracture surface roughness statistics along the direction of crack growth were computed. For the correlation function, these include the Hurst exponent and a cut-off length of the scale invariant regime. We also go beyond the characterization of fracture surface roughness by the correlation function and investigate the scaling of the full statistics of the fracture surface roughness which suggests other possible characterizing parameters. Possible connections between quantitative measures of crack growth resistance and quantitative measures of fracture surface roughness are explored and related to the nature of the ductile crack growth process.

2. Problem formulation and numerical method

A mode I small scale yielding boundary value problem is analyzed for a slice of material having dimensions $h_x \times h_y \times h_z$ and with an initial crack as shown in Fig. 1. The boundary value problem analyzed here is the same as in Needleman et al. (2012), Ponson et al. (2013) and, for completeness, will be briefly described. Further details and additional references are given in Tvergaard and Needleman (2006), Needleman et al. (2012), Ponson et al. (2013). However, here the three dimensional analyses of ductile fracture are carried out using a data parallel implementation.

A convected coordinate Lagrangian formulation is used and all field quantities are taken to be functions of the convected coordinates and time. A Cartesian frame is used in the reference configuration with the coordinates denoted by x_0, y_0 and z_0. Also, x, y and z are used to denote Cartesian coordinates of material points in the deformed configuration. The initial velocity and remote displacement boundary conditions correspond to an isotropic elastic mode I singular field. In addition, symmetry conditions $u_3 = 0$, $T^1 = 0$, $T^2 = 0$ are imposed on $z_0 = 0, h_z$ where $\boldsymbol{u}$ is the displacement vector and $\boldsymbol{T}$ is the traction vector. The finite element calculations are based on the dynamic principle of virtual work written in tensor notation as

$$\int_V \tau^{ij}\delta E_{ij}\, dV = \int_S T^i \delta u_i\, dS - \int_V \rho \frac{\partial^2 u^i}{\partial t^2}\delta u_i\, dV \tag{1}$$

Here, τ^{ij} are the contravariant components of the Kirchhoff stress on the deformed convected coordinate net ($\tau^{ij} = J\sigma^{ij}$, with σ^{ij} being the contravariant components of the Cauchy stress and J being the ratio of the current to reference volume), E_{ij} is the Lagrangian strain tensor, ρ is the mass density, V and S are the volume and surface of the body in the reference configuration.

The block dimensions are $h_x = h_y = 0.4$ m and $h_z = 0.005$ m, with an initial crack tip of opening $b_0 = 1.875 \times 10^{-4}$ m. The finite element mesh consists of 428,256 twenty node brick elements giving 1,868,230 nodes and 5,604,690 degrees of freedom. Ten uniformly spaced elements are used through the thickness h_z. A uniform 208×64 in-plane ($x_0 - y_0$ plane) mesh is used in a 0.02 m $\times$ 0.006 m region immediately in front of the initial crack tip with in-plane elements of dimension 9.62×10^{-5} m by 9.38×10^{-5} m. The element dimension $e_x = 9.62 \times 10^{-5}$ m serves as a normalization length.

Displacements corresponding to the quasi-static mode I isotropic elastic singular displacement field are imposed on the remote boundaries of the region analyzed. Also, the initial velocity field in the region analyzed corresponds to that of the mode I singular field. These initial and boundary conditions aim at providing an approximation to quasi-static response. For quasi-static response, only the ratio of geometric lengths matter, not their absolute magnitude.

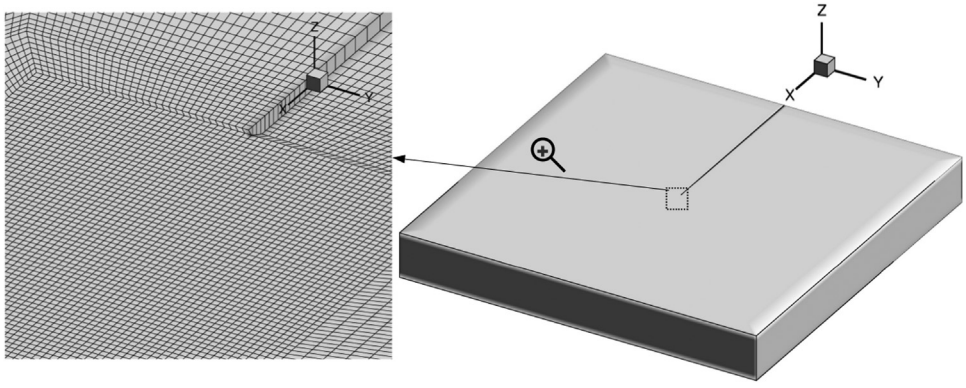

Fig. 1. Sketch of the initially cracked block analyzed and the finite element mesh in the vicinity of the initial crack tip.

The constitutive framework is the modified Gurson constitutive relation (for more details see Tvergaard, 1990) with the rate of deformation tensor written as the sum of an elastic part, $\mathbf{d}^e=\mathbf{L}^{-1}:\hat{\boldsymbol{\sigma}}$, a viscoplastic part, $\mathbf{d}^p$, and a part due to thermal straining, $\mathbf{d}^\Theta=\alpha\dot{\Theta}\mathbf{I}$, so that

$$\mathbf{d}=\mathbf{L}^{-1}:\hat{\boldsymbol{\sigma}}+\alpha\dot{\Theta}\mathbf{I}+\mathbf{d}^p \tag{2}$$

Here, $\hat{\boldsymbol{\sigma}}$ is the Jaumann rate of Cauchy stress, Θ is the temperature, $\alpha=1\times10^{-5}$/K is the thermal expansion coefficient and $\mathbf{L}$ is the tensor of isotropic elastic moduli.

The plastic part of the strain rate, $\mathbf{d}^p$, is given by Pan et al. (1983)

$$\mathbf{d}^p=\left[(1-f)\overline{\sigma}\frac{\dot{\bar{\varepsilon}}}{\boldsymbol{\sigma}:\frac{\partial\Phi}{\partial\boldsymbol{\sigma}}}\right]\frac{\partial\Phi}{\partial\boldsymbol{\sigma}} \tag{3}$$

with the flow potential having the form (Gurson, 1975)

$$\Phi=\frac{\sigma_e^2}{\overline{\sigma}^2}+2q_1f^*\cosh\left(\frac{3q_2\sigma_h}{2\overline{\sigma}}\right)-1-(q_1f^*)^2=0 \tag{4}$$

where $q_1=1.25$, $q_2=1.0$ are parameters introduced in Tvergaard (1981, 1982a), f is the void volume fraction, $\overline{\sigma}$ is the matrix flow strength, and

$$\sigma_e^2=\frac{3}{2}\boldsymbol{\sigma}':\boldsymbol{\sigma}',\quad \sigma_h=\frac{1}{3}\boldsymbol{\sigma}:\mathbf{I},\quad \boldsymbol{\sigma}'=\boldsymbol{\sigma}-\sigma_h\mathbf{I} \tag{5}$$

The function f^*, introduced in Tvergaard and Needleman (1984), is given by

$$f^*=\begin{cases}f, & f<f_c\\ f_c+(1/q_1-f_c)(f-f_c)/(f_f-f_c), & f\geq f_c\end{cases} \tag{6}$$

where the values $f_c=0.12$ and $f_f=0.25$ are used.

The matrix plastic strain rate, $\dot{\bar{\varepsilon}}$, is given by

$$\dot{\bar{\varepsilon}}=\dot{\varepsilon}_0\left[\frac{\overline{\sigma}}{g(\bar{\varepsilon},\Theta)}\right]^{1/m},\quad g(\bar{\varepsilon},\Theta)=\sigma_0G(\Theta)[1+\bar{\varepsilon}/\varepsilon_0]^N \tag{7}$$

with $\bar{\varepsilon}=\int\dot{\bar{\varepsilon}}\,dt$ and $\varepsilon_0=\sigma_0/E$. In Eq. (7) the values of $\dot{\varepsilon}_0=10^3\ \mathrm{s}^{-1}$, $m=0.01$, $N=0.1$, $\sigma_0=300$ MPa and $\varepsilon_0=\sigma_0/E=0.00429$ where $E=70$ GPa. The value of Poisson's ratio, $\nu=0.3$, is used in the calculations.

Adiabatic conditions are assumed so that

$$\rho c_p\frac{\partial\Theta}{\partial t}=\chi\boldsymbol{\tau}:\mathbf{d}^p \tag{8}$$

with $\rho=7600\ \mathrm{kg/m^3}=7.6\times10^{-3}\ \mathrm{MPa/(m/s)^2}$, $c_p=465$ J/(kg °K), $\chi=0.9$, and the temperature-dependence of the flow strength is given by

$$G(\Theta)=1+b_G\exp(-c[\Theta_0-273])[\exp(-c[\Theta-\Theta_0])-1] \tag{9}$$

with $b_G=0.1406$ and $c=0.00793$/K. In Eq. (9), Θ and Θ_0 are in K and $\Theta_0=293$ K. Also, the initial temperature is taken to be uniform and 293 K.

The initial void volume fraction is taken to be zero and the evolution of the void volume fraction is governed by

$$\dot{f}=(1-f)\mathbf{d}^p:\mathbf{I}+\dot{f}_{nucl} \tag{10}$$

where the first term on the right hand side of Eq. (10) accounts for void growth and the second term accounts for void nucleation.

Eight point Gaussian integration is used in each twenty-node element for integrating the internal force contributions and twenty-seven point Gaussian integration is used for the element mass matrix. Lumped masses are used so that the mass matrix is diagonal. The discretized equations are integrated using the explicit Newmark β-method ($\beta=0$) (Belytschko et al., 1976). The constitutive updating is based on the rate tangent modulus method in Peirce et al. (1984), while material failure is implemented via the element vanish technique in Tvergaard (1982b). When the value of the void volume fraction f at an integration point reaches $0.9f_f$, the value of f is kept fixed so that the material deforms with a very small flow strength. The entire element is taken to vanish when three of the eight integration points in the element have reached this stage.

3. Inclusion distributions

In the calculations the material microstructure is characterized by two populations of void nucleating second phase particles: (i) uniformly distributed small particles that are modeled by plastic strain controlled void nucleation; and (ii) large, low strength inclusions that are modeled as “islands” of stress controlled nucleation. In each case, void nucleation is assumed to be described by a normal distribution (Chu and Needleman, 1980).

For plastic strain nucleation

$$\dot{f}_{nucl}^{\text{strain}} = D\dot{\bar{\varepsilon}}, \quad D = \frac{f_N^{\text{strain}}}{s_N^{\text{strain}}\sqrt{2\pi}} \exp\left[-\frac{1}{2}\left(\frac{\bar{\varepsilon}-\varepsilon_N}{s_N^{\text{strain}}}\right)^2\right] \tag{11}$$

with $f_N^{\text{strain}} = 0.04$, $\varepsilon_N = 0.3$ and $s_N^{\text{strain}} = 0.1$.

For stress controlled nucleation

$$\dot{f}_{nucl}^{\text{stress}} = A\left[\dot{\bar{\sigma}} + \dot{\sigma}_h\right], \quad A = \frac{f_N^{\text{stress}}}{s_N^{\text{stress}}\sqrt{2\pi}} \exp\left[-\frac{1}{2}\left(\frac{\bar{\sigma}+\sigma_h-\sigma_N}{s_N^{\text{stress}}}\right)^2\right] \tag{12}$$

if $(\bar{\sigma}+\sigma_h) \geq (\bar{\sigma}+\sigma_h)_{max}$, where the maximum is taken over the previous mechanical history, and $\partial(\bar{\sigma}+\sigma_h)/\partial t > 0$. Otherwise $A = 0$.

The value of f_N^{stress} in Eq. (12) at a point (x_0, y_0, z_0) in the initial undeformed configuration, for an inclusion of radius r_c centered at (x_c, y_c, z_c) is

$$f_N^{\text{stress}} = \begin{cases} \bar{f}_N & \text{for } \sqrt{(x_0-x_c)^2+(y_0-y_c)^2+(z_0-z_c)^2} \leq r_c \\ 0 & \text{for } \sqrt{(x_0-x_c)^2+(y_0-y_c)^2+(z_0-z_c)^2} > r_c \end{cases} \tag{13}$$

The values $\bar{f}_N = 0.04$, $\sigma_N/\sigma_0 = 1.5$ and $s_N^{\text{stress}}/\sigma_0 = 0.2$ are used in the calculations. In Eq. (10) $\dot{f}_{nucl} = \dot{f}_{nucl}^{\text{strain}} + \dot{f}_{nucl}^{\text{stress}}$.

The inclusion radius $r_c = 1.5e_x$ (where e_x is the in-plane element dimension) is kept fixed and the number of inclusions, N_{incl}, in the uniform mesh region in front of the initial crack tip is varied. In terms of e_x the volume, V_u, of the uniform mesh region in front of the initial crack tip is $V_u = 200e_x \times 60e_x \times 50e_x$. The inclusion volume fraction, n, and the mean inclusion spacing, ℓ_0, are given in terms of e_x by $n = \left(N_{incl} \times \frac{4}{3}\pi r_c^3\right)/V_u$ and $\ell_0 = (V_u/N_{incl})^{1/3}$. The location of the inclusion centers within the uniform mesh region in front of the initial crack tip is determined using a random number generator with the restriction that the center to center distance of two neighboring inclusions is at least twice the inclusion radius.

4. Numerical results

A monotonically increasing stress intensity factor, $K_I(t)$, with $\dot{K}_I/(\dot{\varepsilon}_0\sigma_0\sqrt{e_x}) = 1359.4$, is prescribed and calculations continue until the crack approaches the boundary of the uniform mesh region. The calculations are carried out for eight inclusion volume fractions $n = 0.012$, 0.024, 0.036, 0.048, 0.071, 0.095, 0.143 and 0.19 corresponding to mean inclusion spacings $\ell_0 = 10.6e_x$, $8.41e_x$, $7.35e_x$, $6.68e_x$, $5.83e_x$, $5.3e_x$, $4.63e_x$ and $4.21e_x$, respectively. For each inclusion volume fraction, n, calculations are carried out for seven random distributions of inclusion centers (i.e., seven realizations). For $n = 0.012$ crack growth did not occur under small scale yielding conditions for two distributions because no inclusions were sufficiently close to the initial crack front. Hence, for $n = 0.012$ results are presented for five random distributions. A random distribution of inclusions on $z_0 = 0$ and $z_0 = h_z$ is shown in Fig. 2 for $n = 0.024$ ($\ell_0 = 8.41e_x$) while Fig. 3 shows a random distribution for $n = 0.143$ ($\ell_0 = 4.63e_x$).

Curves of normalized crack opening displacement, $b/b_0 - 1$, versus normalized applied J, $J/(\sigma_0 b_0)$, for one realization of each volume fraction, n, are shown in Fig. 4. Here, b is the current crack opening at $x_0 = -2.82e_x$ and $z_0 = h_z$ (there is little dependence of the value of b on z_0). The value of J is computed from the applied stress intensity factor K_I using the small scale yielding relation (Rice, 1968),

$$J = K_I^2 \frac{(1-\nu^2)}{E} \tag{14}$$

In ductile materials significant crack opening and crack tip blunting occurs before crack growth. Under quasi-static mode I small scale yielding conditions, the theoretical value of the slope of the crack opening $(b/b_0 - 1)$ versus $J/(\sigma_0 b_0)$ curve for a blunting crack with the strain hardening parameters used here is about 1/2. The dashed line in Fig. 4 is $(b/b_0 - 1) = 0.5J/(\sigma_0 b_0)$ and agrees very well with the computed J versus crack opening relation prior to the onset of crack growth. This provides an indication that in our dynamic calculations quasi-static loading conditions are reasonably well approximated, at least prior to the onset of crack growth.

In Fig. 5a the white region in $x_0 > 0$ corresponds to $f \geq 0.1$ on the planes along $z_0 = h_z/10$, $h_z/2$ and h_z for one random distribution of inclusions with $n = 0.024$ at $J/(\sigma_0 e_x) = 32.6$ while Fig. 5b shows a similar plot for $n = 0.143$ at $J/(\sigma_0 e_x) = 17.9$. The extent of the $f \geq 0.1$ region along x-axis is defined as the projected crack length in a plane. Subsequently, the overall amount of crack growth, $\Delta a(t)$, is defined as the mean projected crack length for ten uniformly spaced planes through the thickness. Although $f = 0.1$ has no special significance in the constitutive relation, it gives a representative picture of the current crack tip as noted by Needleman and Tvergaard (1987), Becker et al. (1989). In Fig. 5a, for $n = 0.024$, $\Delta a \approx 178e_x$ and in Fig. 5b, for $n = 0.143$, $\Delta a \approx 175e_x$. In all six plots in Fig. 5 the extent of the frame is $x_0 = 200e_x$ which is the end of the fine mesh region.

For $n = 0.024$, where inclusions are relatively far away from each other ($\ell_0 = 8.41e_x$) shear localization plays a significant role in linking voids nucleated from the larger inclusions as evident from the extent of zig-zag in the crack path shown in Fig. 5a. For $n = 0.143$ ($\ell_0 = 4.63e_x$) the abundance of inclusions ahead of the crack tip facilitates crack growth along the initial crack plane and the extent of zig-zag is limited as seen in Fig. 5b.

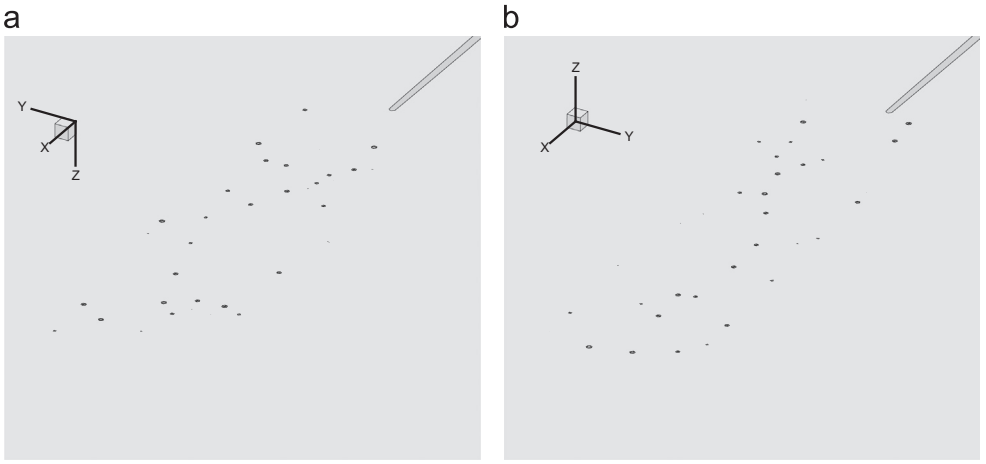

Fig. 2. One initial random distribution of inclusions ahead of the initial crack tip for the inclusion volume fraction $n=0.024$ ($\ell_0 = 8.41e_x$). (a) $z_0 = 0$. (b) $z_0 = h_z$.

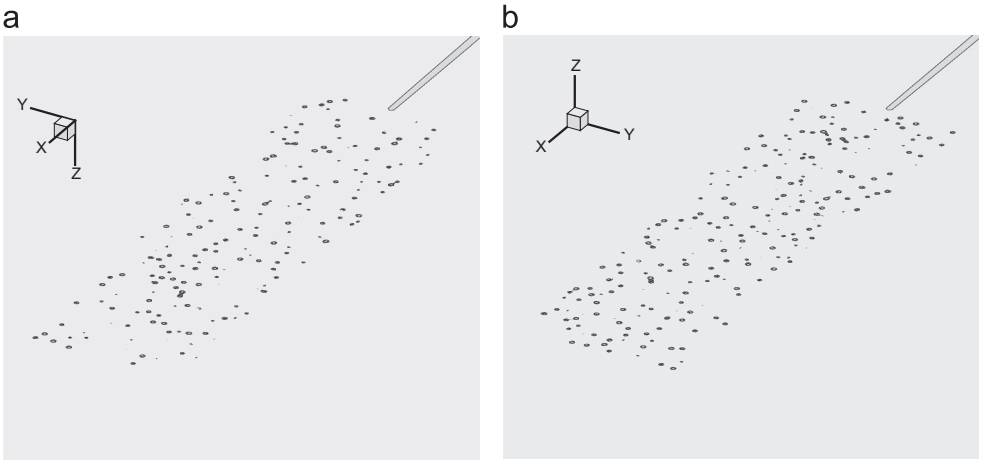

Fig. 3. One initial random distribution of inclusions ahead of the initial crack tip for the inclusion volume fraction $n=0.143$ ($\ell_0 = 4.63e_x$). (a) $z_0 = 0$. (b) $z_0 = h_z$.

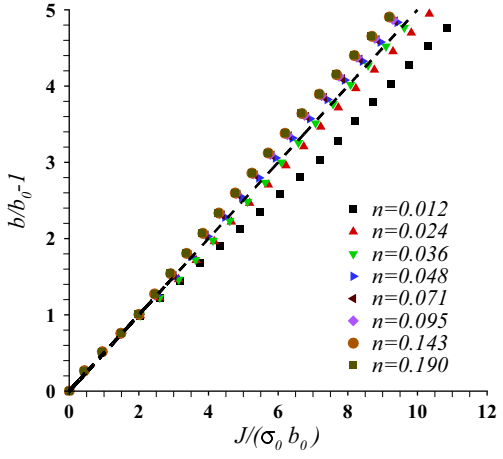

Fig. 4. Curves of normalized crack opening displacement, $b/b_0 - 1$, versus normalized applied J, $J/(\sigma_0 b_0)$, for one random distribution of inclusions for each of the eight inclusion volume fractions n considered.

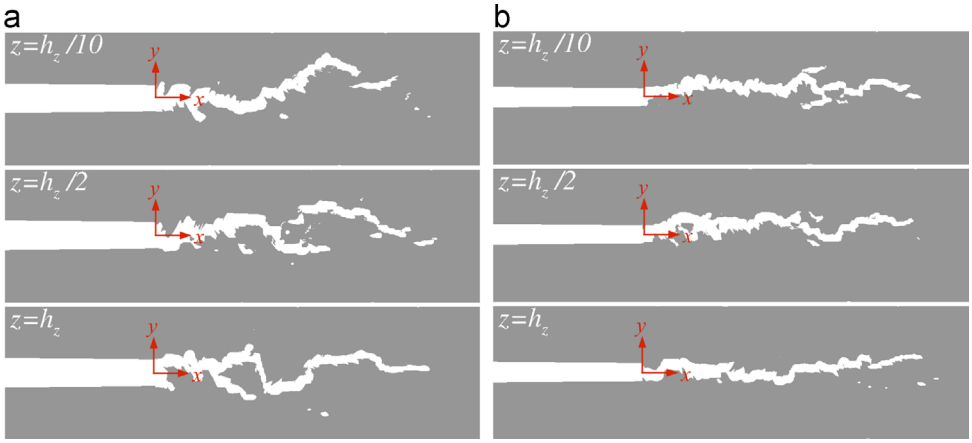

Fig. 5. The white region for $x_0>0$ corresponds to values of void volume fraction $f\geq 0.1$ on three parallel planes through the thickness ($z=$ constant) for one random distribution of: (a) an inclusion volume fraction $n=0.024$ ($\ell_0=8.41e_x$) and (b) an inclusion volume fraction $n=0.143$ ($\ell_0=4.63e_x$).

4.1. Crack growth resistance

Crack growth resistance curves, $J-R$ curves, for all seven inclusion distributions with $n=0.024$ and with $n=0.143$ are shown in Fig. 6. The value of J is normalized by $\sigma_0 e_x$ and the crack length Δa is normalized by e_x. As seen in Fig. 6 both the level and the slope of the $J-R$ curve is greater for the smaller volume fraction of inclusions. The variation in the $J-R$ curves for the seven random distributions of inclusions for $n=0.024$, Fig. 6a, mainly stems from the initial stage of crack growth. The initiation of crack growth depends on the interaction of the initial crack front with the nearest inclusions and for fewer inclusions as with $n=0.024$ there is a significant variation among the various realizations. On the other hand, for $n=0.143$, Fig. 6b, the variation in the $J-R$ curves for the seven random distributions of inclusions is small.

The value of J_{IC}, a measure of crack initiation toughness, is defined by a procedure outlined in the ASTM E1820-11 (2011) standard. Here, we use the procedure illustrated in Fig. 7a which mimics the ASTM E1820-11 (2011) standard. As shown in Fig. 7a, a power law of the form $J/(\sigma_0 e_x)=A(\Delta a/e_x)^B$ is fit to the portion of the $J-R$ curve in between two exclusion lines, where the exclusion lines are $J/e_x=2\sigma_0(\Delta a/e_x-1.5)$ and $J/e_x=2\sigma_0(\Delta a/e_x-15)$. The value of normalized fracture toughness $J_{IC}/(\sigma_0 e_x)$ is defined as the intersection of the curve $J/(\sigma_0 e_x)=A(\Delta a/e_x)^B$ and the line $J/e_x=2\sigma_0(\Delta a/e_x-2)$. The variation of $J_{IC}/(\sigma_0 e_x)$ with n is shown in Fig. 7b. The error bars in Fig. 7b show the standard errors for realizations of inclusion distributions having the same value of n. The standard error, R_s, of a variable, X, is given by

$$R_s=\frac{\left(\frac{1}{N_R-1}\sum_{i=1}^{N_R}(X_i-\overline{X})^2\right)^{1/2}}{\sqrt{N_R}} \tag{15}$$

Here, N_R is the number of realizations of the variable X. As seen in Fig. 7b, the value of $J_{IC}/(\sigma_0 e_x)$ decreases rapidly with increasing n for $n\leq 0.071$ and then decreases slowly, being nearly the same value for $n=0.143$ and $n=0.19$. The variation of $J_{IC}/(\sigma_0 e_x)$ with the mean inclusion spacing, ℓ_0/e_x, is shown in Fig. 7c. Two distinct regions can be identified. For $\ell_0<\approx 6e_x$, the value of $J_{IC}/(\sigma_0 e_x)$ increases linearly with one slope while for $\ell_0\geq\approx 6e_x$, $J_{IC}/(\sigma_0 e_x)$ increases linearly with ℓ_0/e_x with a much larger slope. As will be discussed subsequently, there is a qualitative change in the nature of the crack growth process at $\ell_0\approx 6e_x$ ($n\approx 0.07$).

Another quantity that characterizes crack growth resistance is the non-dimensional tearing modulus (Paris et al., 1979),

$$T_R=\left(\frac{E}{\sigma_0^2}\right)\frac{dJ}{d(\Delta a)} \tag{16}$$

As seen in Fig. 6, after some crack growth the $J-R$ curves are nearly linear and the tearing modulus, T_R, is calculated from the slope of a line fit to the portion of the $J-R$ curve $100\leq\Delta a/e_x\leq 150$. The variation of T_R with n and ℓ_0/e_x is shown in Fig. 8a and b. The error bars in Fig. 8 show the standard errors for realizations of inclusion distributions having the same value of n and ℓ_0/e_x. The variation of T_R with n and ℓ_0/e_x in Fig. 8a and b is similar to that in Fig. 7b and c for $J_{IC}/(\sigma_0 e_x)$. In particular, in Fig. 8b there is a bilinear dependence on ℓ_0/e_x with a transition in slope at $\ell_0\approx 6e_x$. Fig. 8c and d shows the variation of T_R with J_{IC} normalized in two ways: in Fig. 8c J_{IC} is normalized by e_x which is a fixed length for all volume fractions n, while in Fig. 8d J_{IC} is normalized by the mean inclusion spacing, ℓ_0 which, of course, varies with inclusion volume fraction n. In Fig. 8c J_{IC} and T_R are linearly related for all volume fractions, whereas in Fig. 8d the linear relation between J_{IC} and T_R breaks down for smaller values of T_R that correspond to larger values of n or, equivalently, to smaller values of ℓ_0. Thus, regardless of the normalization, the dependence of T_R on inclusion volume fraction n or spacing ℓ_0 is the same as for J_{IC} for smaller values of n (lager values of ℓ_0).

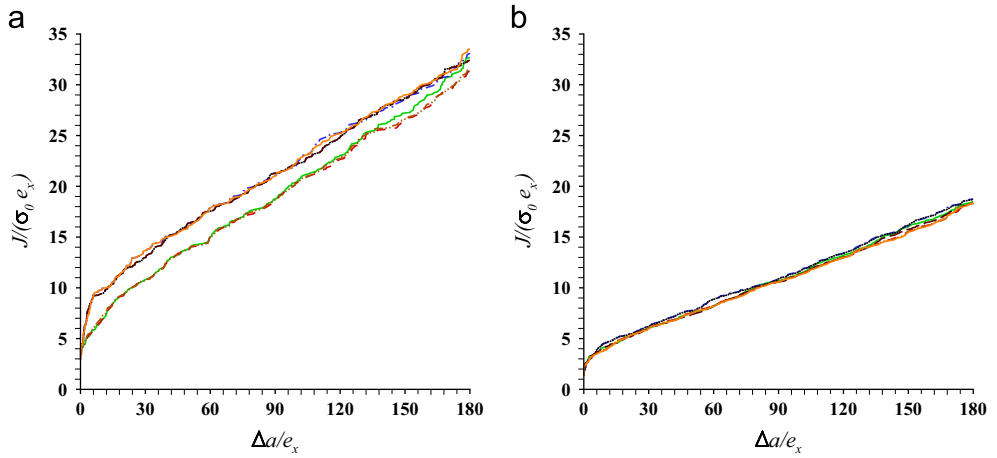

Fig. 6. Applied normalized J, $J/(\sigma_0 e_x)$, versus normalized crack extension, $\Delta a/e_x$, for seven random distributions of inclusions for: (a) an inclusion volume fraction $n=0.024$ ($\ell_0 = 8.41 e_x$) and (b) an inclusion volume fraction $n=0.143$ ($\ell_0 = 4.63 e_x$).

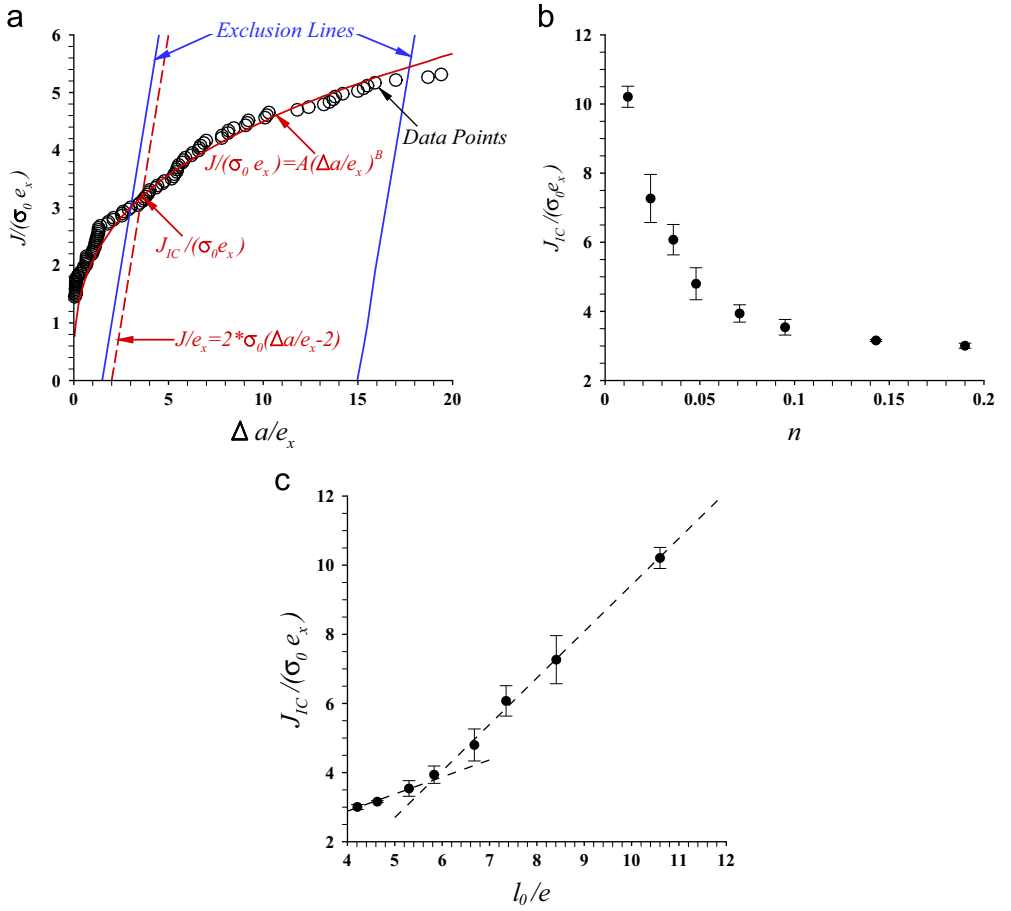

Fig. 7. (a) Illustration of the calculation of $J_{IC}/(\sigma_0 e_x)$, from the $J-R$ curve for one random distribution of inclusions with $n=0.143$ ($\ell_0 = 4.63 e_x$). (b) Variation of $J_{IC}/(\sigma_0 e_x)$ with inclusion volume fraction n. (c) Variation of $J_{IC}/(\sigma_0 e_x)$ with mean inclusion spacing ℓ_o/e_x.

4.2. Statistical analysis of fracture surfaces

To calculate the full fracture surface statistics, the deformed finite element mesh on ten $z=$ constant planes is projected onto a uniform grid in the $x-y$ plane (with (x,y,z) denoting the current positions of material points in a Cartesian frame)

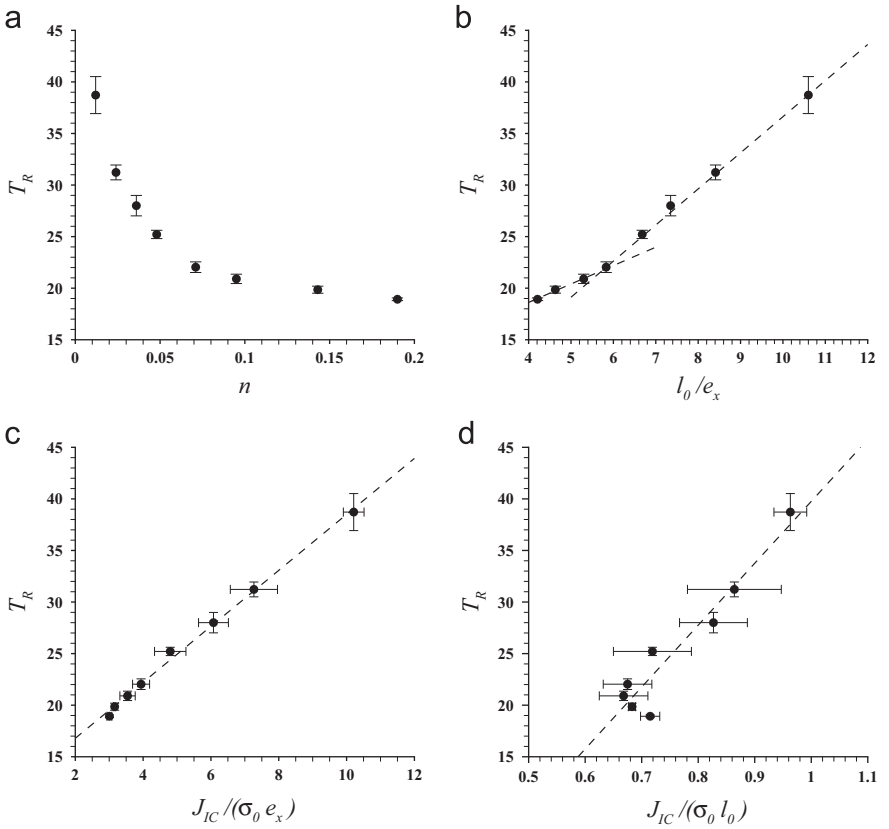

Fig. 8. (a) Variation of the tearing modulus, T_R, with inclusion volume fraction n. (b) Variation of the tearing modulus, T_R, with mean inclusion spacing ℓ_o/e_x. (c) Variation of the tearing modulus, T_R, with $J_{IC}/(\sigma_0 e_x)$. (d) Variation of the tearing modulus, T_R, with $J_{IC}/(\sigma_0 \ell_0)$.

having a grid spacing of $e_x/2 \times e_x/2$ (for the 20-node elements in the uniform region $e_x/2$ is the distance between mesh points in the x-direction in the undeformed configuration). This uniform grid was superimposed on top of the deformed finite element mesh and the value of the void volume fraction f on a grid point was interpolated from the four nearest neighbors taken from each of the four quadrants around that grid point. The fracture surface is then defined by a continuous $f=0.1$ contour connected to the initial crack tip on all ten $z=$ constant planes. The fracture surface roughness, $h(x,z)$, is computed when there are continuous $f=0.1$ contours of projected length $\geq 170e_x$ in the x-direction in all ten planes (as noted in Ponson et al., 2013 the fracture surface scaling is not sensitive to the value of f used to define the fracture surface). For each calculation there are two fracture surfaces, top and bottom, in the $x-z$ plane having dimensions $170e_x \times h_z$. In each of the ten planes, the top fracture surface roughness, $h^{top}(x,z)$, is the y coordinate at a point (x, z) above the crack for which $f=0.1$ and $h^{bot}(x,z)$ is the y coordinate at a point (x, z) below the crack for which $f=0.1$. This procedure mimics a profilometer.

Attention is confined to calculating fracture surface roughness in the direction of crack propagation, the x-direction, because the slab analyzed is too thin to allow a statistical analysis of roughness parallel to the crack front. The height fluctuations of the fracture surface are characterized by the correlation function, Δh, defined as

$$\Delta h(\delta x) = \sqrt{\langle [h(x+\delta x, z) - h(x,z)]^2 \rangle_{x,z}} \tag{17}$$

Here, $\langle\ \rangle_{x,z}$ denotes the average over x and z. The quantity $\Delta h(\delta x)$ can be interpreted as the typical difference of height between two points separated by a distance δx along the mean fracture plane. The correlation function is computed for both top and bottom fracture surfaces and the final correlation function is obtained by averaging over both surfaces.

Log–log plots of the correlation function $\Delta h(\delta x)$ for seven random distributions of inclusions with an inclusion volume fraction $n=0.024$ are shown in Fig. 9a and corresponding plots for $n=0.143$ are shown in Fig. 9b. The correlation functions exhibit power law behavior

$$\Delta h(\delta x) \propto \delta x^{\beta} \tag{18}$$

where β is the Hurst exponent. The Hurst exponent β lies between 0 and 1, with $\beta = 1/2$ corresponding to a random walk. For $\beta > 1/2$, an increase (decrease) is likely to be followed by an increase (decrease); for $\beta < 1/2$ an increase (decrease) is likely to be followed by a decrease (increase).

The value of β is calculated as the slope of the dashed line fit to the range $\delta x < 4e_x$ to the Δh versus δx curve on the log–log plot as illustrated in Fig. 9. The computed values of β for various values of inclusion volume fraction n are shown in Fig. 9c. The average value is $\beta = 0.53$ with an standard error of 0.0023. For all values of n, the power law behavior holds for nearly two orders of magnitude of size scale and then breaks down for $\delta x > \xi$ as seen in Fig. 9. Thus, the correlation function $\Delta h(\delta x)$ exhibits two regimes, $\beta \approx 0.53$ for $\delta x < \xi$ and $\beta \approx 0$ (on average) for $\delta x > \xi$. The value of the cut-off length, ξ, is defined as the intersection of $\Delta h(\delta x) = \Delta h_s$ line with the line fit to the linear portion of the log–log plot as illustrated in Fig. 9.

The dependence of the cut-off length, ξ, and the saturation value of the correlation function, Δh_s, on the inclusion volume fraction n and mean inclusion spacing ℓ_0/e_x is shown in Fig. 10. As can be seen in the figures the values of ξ and Δh_s do vary with n or equivalently with ℓ_0/e_x. The error bars shown in Fig. 10 are the standard errors for realizations of inclusion distributions having the same n and ℓ_0/e_x. The variation of both ξ and Δh_s with n, Fig. 10a and c, and with ℓ_0/e_x, Fig. 10b and d, is qualitatively similar to the variations of J_{IC}, Fig. 7b and c, and T_R, Fig. 8a and b, with both n and ℓ_0/e_x at least for $n < \approx 0.07$ or equivalently $\ell_0 > \approx 6e_x$.

In Vernède et al. (submitted for publication) the full statistics of fracture surface height fluctuations were obtained for cracks in a variety of materials and it was found that the deviation from Gaussian statistics was material dependent. Therefore, here, in order to explore possible effects of inclusion volume fraction on the predicted fracture surface morphology the full statistics of the height variation $\delta h(x,z)$ is investigated. The height variation $\delta h(x,z)$ is defined as

$$\delta h(x,z) = h(x+\delta x,z) - h(x,z) \tag{19}$$

In Eq. (19), the roughness $h(x,z)$ is the average roughness of the fracture surfaces obtained for all realizations for a given inclusion volume fraction n.

As in Ponson et al. (2013), the procedure used to compute the histogram probability density $p(\delta h|\delta x)$ is

1. The value of δx is fixed.
2. For each location (x, z) on both the top and bottom fracture surfaces, the corresponding height variations δh are computed. This procedure results in a set $\{\delta h\}_{\delta x}$ of height variations for the fixed scale δx.

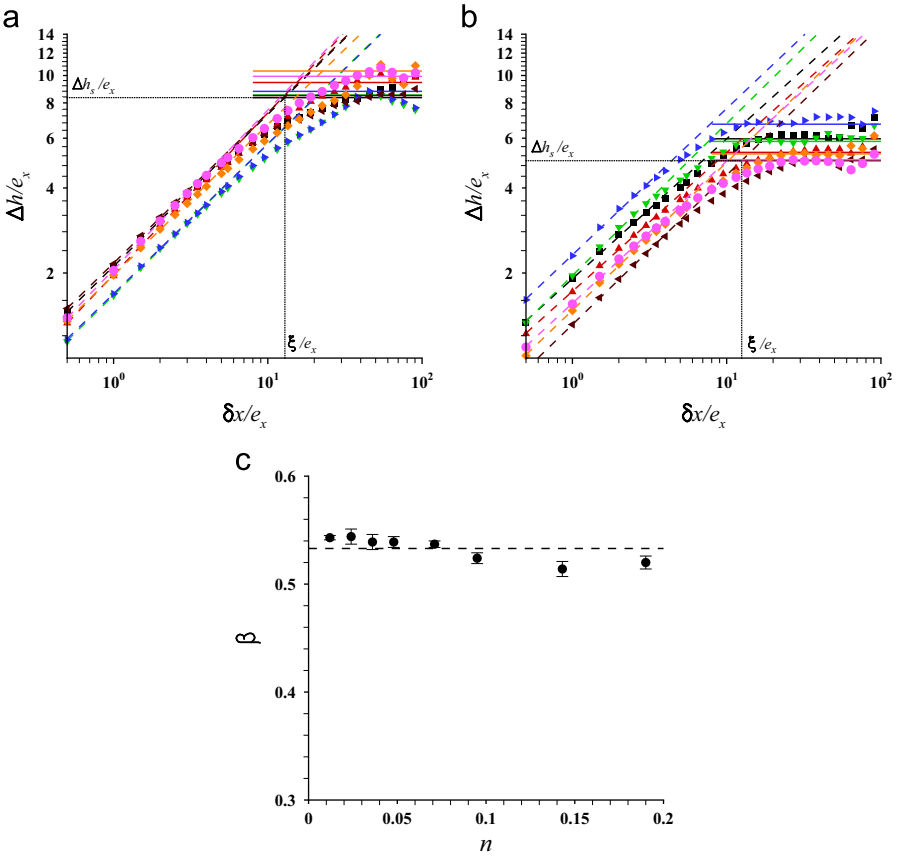

Fig. 9. Height–height correlation functions of the fracture surface roughness. (a) Seven realizations with inclusion volume fraction $n=0.024$ ($\ell_0/e_x = 8.41$). (b) Seven realizations with inclusion volume fraction $n=0.143$ ($\ell_0/e_x = 4.63$). (c) Variation of the roughness exponent β with n.

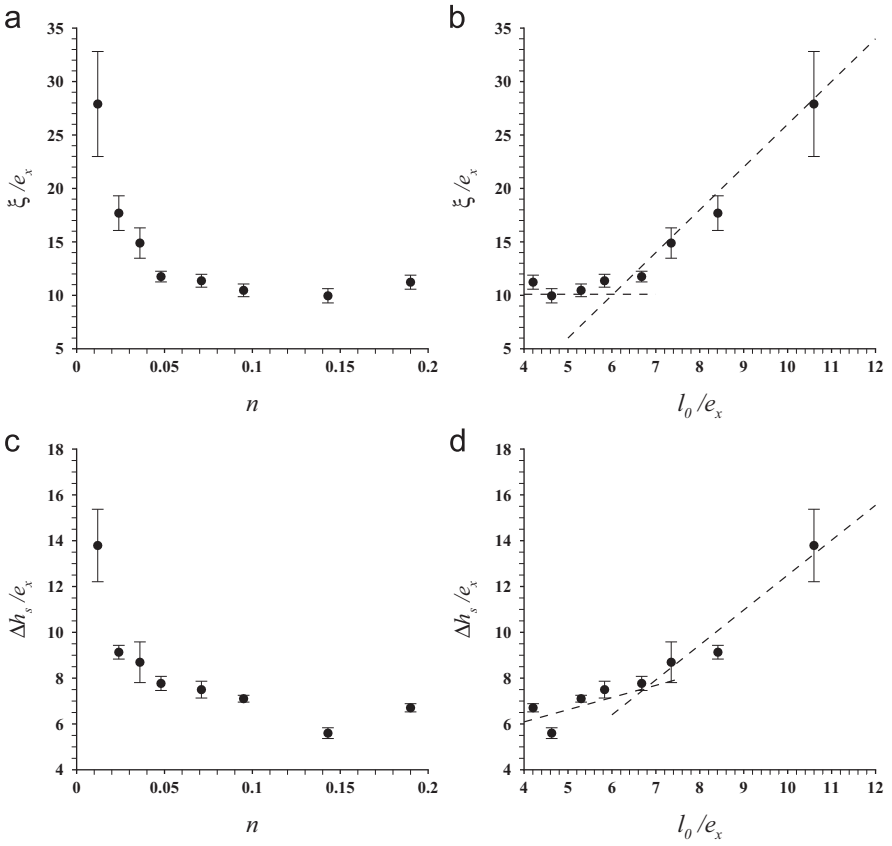

Fig. 10. (a) Variation of the normalized cut-off length, ξ/e_x, with the inclusion volume fraction n. (b) Variation of the normalized cut-off length, ξ/e_x, with mean inclusion spacing ℓ_o/e_x. (c) Variation of the normalized saturation value of the correlation function, $\Delta h_s/e_x$, with n. (d) Variation of the normalized saturation value of the correlation function, $\Delta h_s/e_x$, with ℓ_o/e_x.

3. The histogram for this set of values is computed. The histogram of δh is calculated by placing the values of δh into 'boxes' $[b_{\min}b_2]$, $[b_2b_3]$, ..., $[b_{n-1}b_{\max}]$ where the side b_1, b_2 of the boxes are distributed homogeneously between $b_{\min}=\min[\delta h]$ and $b_{\max}=\max[\delta h]$.
4. The histogram probability density is calculated as the fraction of values of δh contained in the ith box.

This procedure is repeated for several values of δx. An important property is that the standard deviation of $p(\delta h|\delta x)$ is the correlation function $\Delta h(\delta x)$.

The distribution $p(\delta h|\delta x)$ is shown for three values of δx in Fig. 11a for an inclusion volume fraction $n=0.024$ and in Fig. 11b for $n=0.143$. In both plots the larger the value of δx, the broader the distribution, as expected from the scaling of the correlation function $\Delta h(\delta x)\propto \delta x^{\beta}$.

The distributions in Fig. 11 are not Gaussian, but exhibit fat tails for larger values of δh. This implies that large fluctuations are not exponentially rare on ductile fracture surfaces as is the case for brittle fracture surfaces (Ponson et al., 2007). However, at sufficiently large scales δx, the roughness statistics is expected to recover a Gaussian behavior, as seen in Vernède et al. (submitted for publication). To describe this effect more quantitatively, the distributions $p(\delta h)$ are described using a family of probability distributions referred to as Student's t-distribution

$$p_{k,\delta h_c}(\delta h)\propto \frac{1}{\delta h_c}\left(1+\frac{1}{k}\left(\frac{\delta h}{\delta h_c}\right)^2\right)^{-(k+1)/2} \tag{20}$$

where k is a dimensionless parameter and δh_c is a scale factor. Student's t-distribution function has a power law tail $p(\delta h)\propto \delta h^{-(k+1)}$ and approaches a Gaussian as k tends to infinity. The fits to Student's t-distribution are given by the solid lines in Fig. 11 for three values of δx with the fitting restricted to values of $\delta x/e_x<10$.

The parameter k in Eq. (20) characterizes the shape of the distribution. However, it is more convenient to consider the parameter $\sqrt{k/(k-2)}$ instead of k (Ponson et al., 2013). The variation of $\sqrt{k/(k-2)}$ with δx for the smallest and largest inclusion volume fractions, $n=0.012$ and $n=0.190$, considered are shown in Fig. 12a on a logarithmic scale. As shown in Fig. 12a, $\sqrt{k/(k-2)}\propto \delta x^{-\mu}$ with $\mu=0.165$ for $n=0.012$ and with $\mu=0.193$ for $n=0.190$. As k tends to infinity

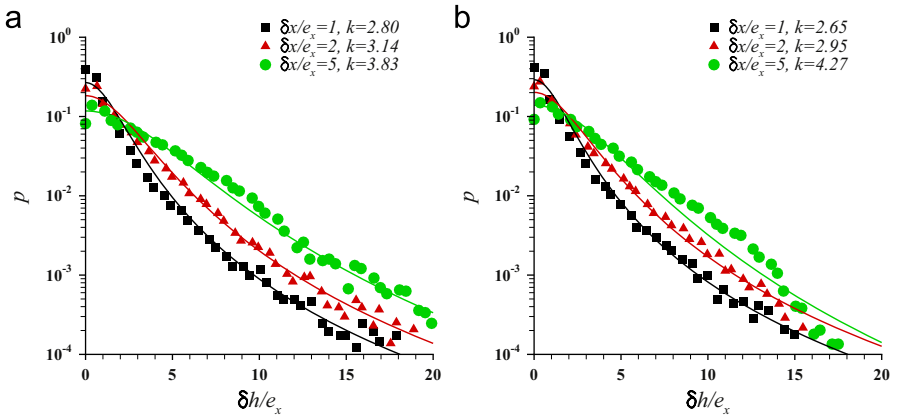

Fig. 11. Histograms $p(\delta h|\delta x)$ of height variations δh, Eq. (19), for various values of δx. (a) Inclusion volume fraction $n=0.024$. (b) Inclusion volume fraction $n=0.143$. The solid lines are a fit based on Student's t-distribution, Eq. (20), using various values of the parameter k. The values plotted are averages for all realizations having the same value of n.

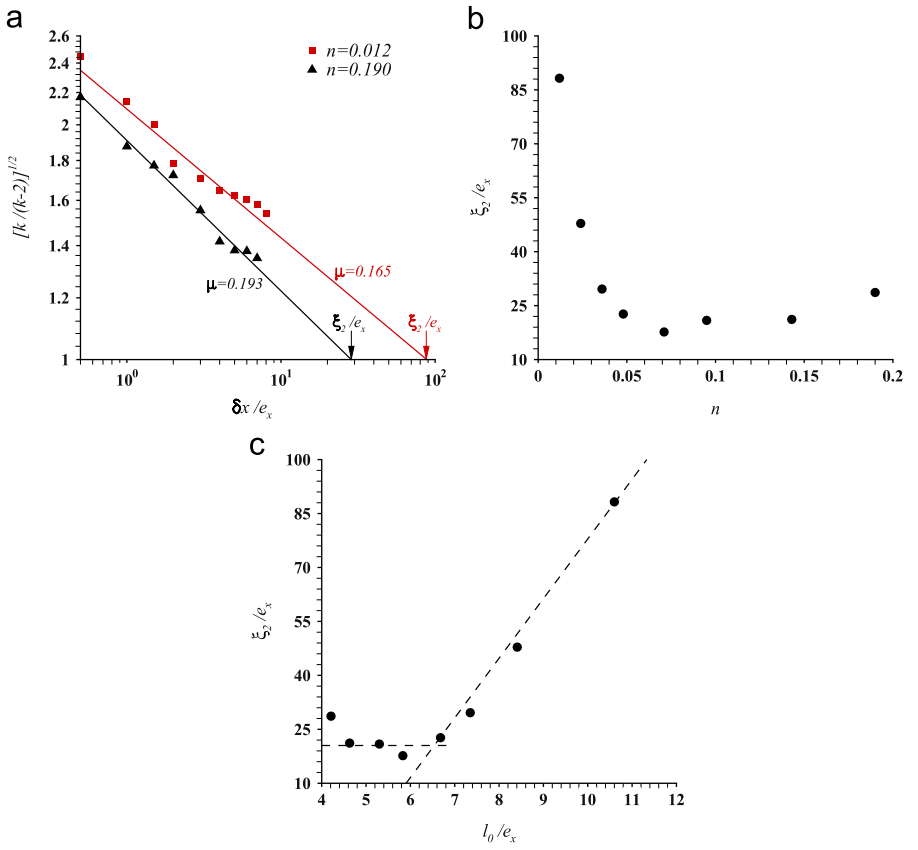

Fig. 12. (a) Variations of the parameter $\sqrt{k/(k-2)}$ obtained from the fit of Student's t-distribution function to p versus δh plots as shown in Fig. 11 with length scale δx. (b) Variation of ξ_2 with inclusion volume fraction n. (c) Variation of ξ_2 with mean inclusion spacing ℓ_0/e_x. The value of ξ_2 is the value of δx at which $\sqrt{k/(k-2)} \simeq 1$. The values plotted are averages for all realizations having the same value of n.

(the Gaussian limit), $\sqrt{k/(k-2)} \simeq 1$. Extrapolating the power law behavior $\sqrt{k/(k-2)} \propto \delta x^{-\mu}$ to larger values of δx, gives $\sqrt{k/(k-2)}_{(\delta x = \xi_2)} \simeq 1$ at the cross-over length $\delta x = \xi_2$ as shown in Fig. 12a. This suggests that for $\delta x > \xi_2$ Gaussian statistics are recovered for the fracture surface roughness. The dependence of the cross-over length ξ_2 on inclusion volume fraction n and mean inclusion spacing ℓ_0/e_x are shown in Fig. 12b and c. The generally decreasing trend of ξ_2 with increasing inclusion volume fraction n or equivalently decreasing mean inclusion spacing ℓ_0/e_x is seen in Fig. 12b and c. Figs. 12b and c show that with increasing n (decreasing ℓ_0) Gaussian statistics are recovered at a smaller cross-over length ξ_2.

5. Toughness–roughness correlation

The variation of the normalized cut-off length, ξ/e_x, with the normalized fracture toughness, $J_{IC}/(\sigma_0 e_x)$, and the variation of the normalized saturation value of the correlation function, $\Delta h_s/e_x$, with $J_{IC}/(\sigma_0 e_x)$ are shown in Fig. 13a and b respectively. The dashed lines in Fig. 13 are linear least square fits to the values for inclusion volume fractions $n \le 0.071$ ($\ell_0 \ge 5.83 e_x$). For $n \le 0.071$ there is a linear correlation between ξ and Δh_s, measures of fracture surface roughness, with J_{IC}, a measure of fracture toughness. This linear correlation breaks down for $n > 0.071$.

The variations of ξ/e_x and $\Delta h_s/e_x$ with the tearing modulus, T_R, are shown in Fig. 14. Here also the dashed lines in Fig. 14 are linear least square fits to the values for $n \le 0.071$ ($\ell_0 \ge 5.83 e_x$). The variations of ξ/e_x and $\Delta h_s/e_x$ with T_R in Fig. 14 show a similar trend as in Fig. 13 which stems from the fact that T_R is linearly correlated with $J_{IC}/(\sigma_0 e_x)$ (see Fig. 8c).

The variation of the normalized cross-over length, ξ_2/e_x, with $J_{IC}/(\sigma_0 e_x)$ is shown in Fig. 15a and the variation of ξ_2/e_x with T_R is shown in Fig. 15b. The dashed line in Fig. 15 is a linear least square fit to the values corresponding to inclusion volume fractions $n \le 0.071$ ($\ell_0 \ge 5.83 e_x$) to illustrate the trend. The cross-over length, ξ_2, is calculated as an average over all realizations with the same inclusion volume fraction n. Here also the variations of ξ_2/e_x with $J_{IC}/(\sigma_0 e_x)$ and T_R are approximately linear for smaller n with the linear correlation breaking down for larger values of n.

The values of the roughness measures ξ, ξ_2 and Δh_s all correlate with a toughness measure, J_{IC} or T_R, for a sufficiently small volume fraction of void nucleating inclusions, $n \le 0.071$ (or equivalently sufficiently large mean inclusion spacings $\ell_0 \ge 5.83 e_x$) in the calculations here. The correlation of Δh_s with J_{IC} and T_R extends to somewhat smaller values of n in Fig. 13b and 14b.

The difference in response between a relatively small fraction of void nucleating inclusions and larger volume fractions can be understood in terms of the model of Tvergaard and Hutchinson (2002) who carried out a plane strain calculation for a string of voids in front of an initial crack in a J_2-flow theory solid. They found that for small volume fractions, crack growth could be considered to occur by a void-by-void mechanism whereas for larger volume fractions crack growth would involve

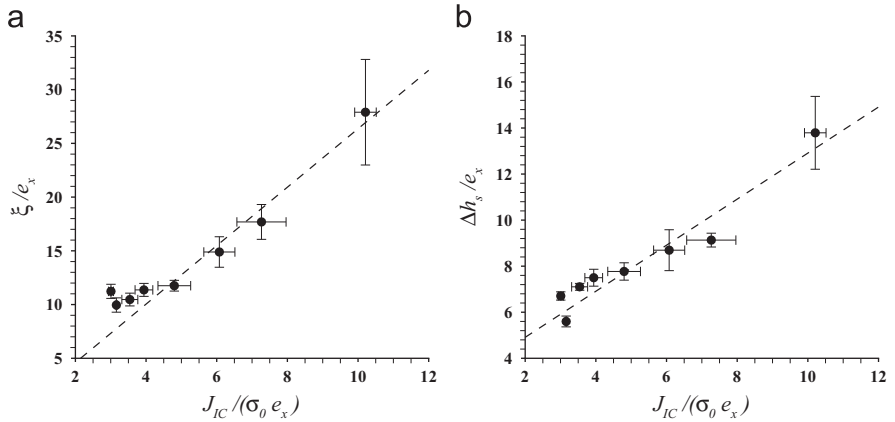

Fig. 13. (a) Variation of the normalized cut-off length ξ/e_x with $J_{IC}/(\sigma_0 e_x)$. (b) Variation of the normalized saturation value of the correlation function $\Delta h_s/e_x$ with $J_{IC}/(\sigma_0 e_x)$. The slope of the dashed lines in (a) is 2.72 and in (b) is 1.00.

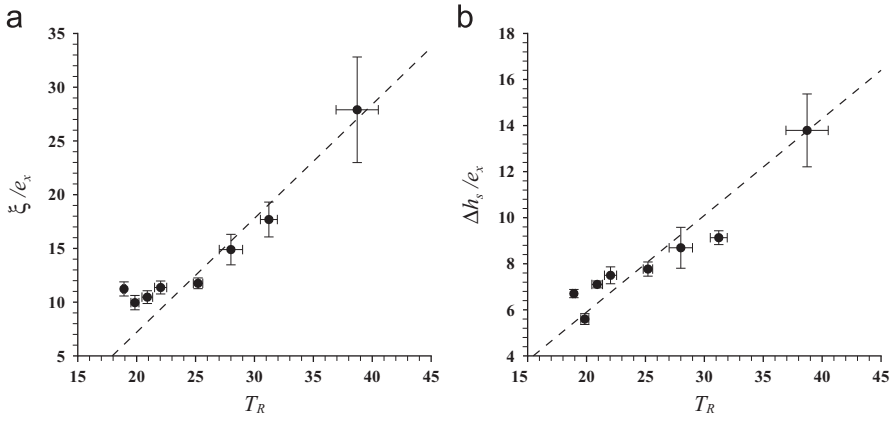

Fig. 14. (a) Variation of the normalized cut-off length ξ/e_x with tearing modulus T_R. (b) Variation of the normalized saturation value of the correlation function $\Delta h_s/e_x$ with tearing modulus T_R. The slope of the dashed line in (a) is 1.06 and in (b) is 0.42.

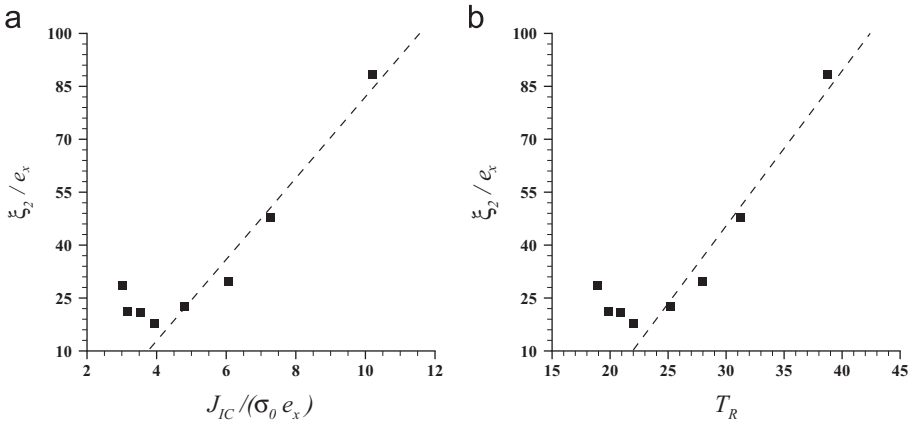

Fig. 15. (a) Variation of the normalized cross-over length ξ_2/e_x with $J_{IC}/(\sigma_0 e_x)$. (b) Variation of ξ_2/e_x with tearing modulus T_R. The values of ξ_2 are averages for all realizations having the same value of n. The slope of the dashed line in (a) is 11.5 and in (b) is 4.4.

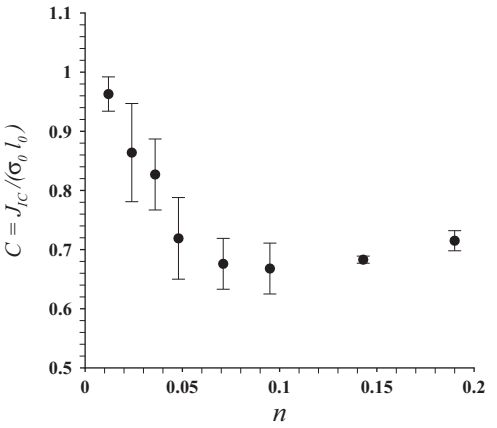

Fig. 16. Variation of the parameter $C = J_{IC}/(\sigma_0 \ell_0)$ introduced by Tvergaard and Hutchinson (2002) with inclusion volume fraction n.

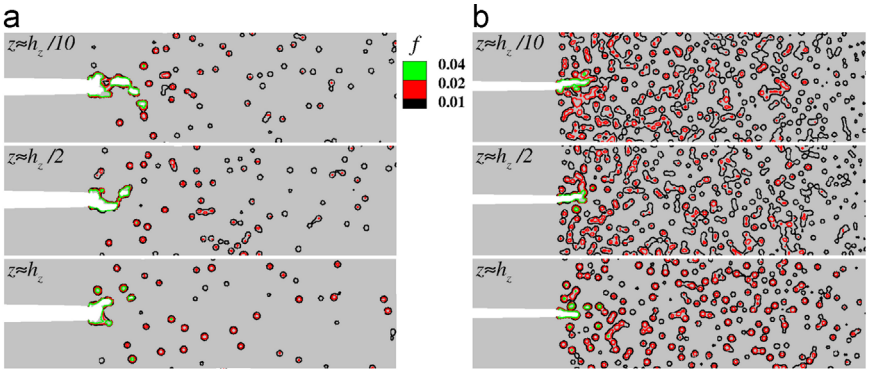

Fig. 17. Contours of void volume fraction f on three parallel planes through the thickness ($z =$ constant planes) at $J/J_{IC} \approx 1.4$. (a) For an inclusion volume fraction $n = 0.024$ ($\ell_0 = 8.41 e_x$). (b) For an inclusion volume fraction $n = 0.143$ ($\ell_0 = 4.63 e_x$).

multiple void interactions. They characterized the response in terms of a dimensionless parameter $C = J_{IC}/(\sigma_0 \ell_0)$. Since the calculations in Tvergaard and Hutchinson (2002) were for a J_2-flow theory solid, crack growth did not actually occur and J_{IC} was identified with a specified ligament reduction between the initial crack tip and the closest void. Larger values of C, $C \approx 1$, corresponded to void-by-void crack growth and smaller values, $C \approx 0.5$, to multiple void interaction crack growth. The

variation of C with inclusion volume fraction n in our calculations is shown in Fig. 16 where $C \approx 1.0$ for $n=0.012$ and decreases to $C \approx 0.68$ for $n \geq 0.071$. The values of C in Fig. 16 are affected by the fact that in our calculations the voids nucleate after some deformation. Nevertheless, these values of C suggest that void-by-void crack growth is dominant for $n < 0.071$ or $\ell_0 > 5.83 e_x$ whereas multiple void interaction crack growth is dominant for $n > 0.071$ or $\ell_0 < 5.83 e_x$.

Fig. 17 shows contours of void volume fraction f on three planes through the thickness for two calculations, one with $n=0.024$ ($\ell_0 = 8.41 e_x$) and the other with $n=0.143$ ($\ell_0 = 4.63 e_x$), both at $J/J_{IC} \approx 1.4$. In Fig. 17a for $n=0.024$, inter-void interactions among the voids nucleated ahead of the crack tip are limited whereas for $n=0.143$, Fig. 17b, multiple voids have nucleated ahead of the crack tip and have started to interact. This will eventually lead to the formation of micro-cracks. The transition from void-by-void crack growth to multiple void interaction crack growth is associated with: (i) values of J_{IC} and T_R that are nearly independent of inclusion volume fraction n, Figs. 7b and 8a; (ii) deviation from a linear correlation between crack growth resistance measures and fracture surface roughness measures, Figs. 13–15; and (iii) a bilinear dependence of J_{IC} and T_R on ℓ_0/e_x with a transition in slope at $\ell_0 \approx 6 e_x$ as shown in Figs. 7c and 8b. Thus, our results indicate that for ductile fracture (fracture by the nucleation, growth and coalescence of voids) a linear correlation between toughness measures and fracture surface roughness measures is expected for void-by-void crack growth but not for multiple void interaction crack growth.

6. Discussion

Three dimensional ductile crack growth has been analyzed for fixed material and fracture properties for volume fractions of randomly distributed void nucleating inclusions ranging from 1% to 19%. For each volume fraction, calculations were carried out for seven realizations permitting effects of statistical variations in inclusion locations to be assessed (for $n=0.012$ or $\ell_0 = 10.6 e_x$ crack growth occurred under small scale yielding conditions only for five of the realizations). Sufficient crack growth was computed to: (i) calculate J_{IC}, by a procedure mimicking the ASTM standard, and the tearing modulus T_R; and (ii) calculate the fracture surface roughness by a procedure mimicking that used in experiments, see Bouchaud (1997), Vernède et al. (submitted for publication). To the extent that our simulations provide a physically realistic model of fracture in a microstructure where the ductile fracture process involves two populations of void nucleating particles (larger inclusions that nucleate voids at small strains and smaller particles that nucleate voids at larger strains), our results show the effect of variations of a single microstructural feature, the volume fraction (or mean spacing) of inclusions, on crack growth resistance and fracture surface roughness.

Although our focus is on the features of ductile fracture toughness and fracture surface roughness, the question arises as to the extent to which our model provides physically realistic predictions. The values of E, ν and σ_0 used in the calculations are representative of aluminum alloys (except for the density, which was taken to be greater than that for aluminum to reduce the stable time step). The value of K_{IC}, computed using Eq. (14) from the value of J_{IC} in Fig. 6 depends on the value assigned to e_x. With e_x taken as $\approx 100\,\mu$m, the value of K_{IC} ranges from ≈ 150 MPa$\sqrt{\text{m}}$ for an inclusion volume fraction, n, of 1.2% to ≈ 80 MPa$\sqrt{\text{m}}$ for $n=19\%$. Representative values of K_{IC} for a variety of Al alloys fall in a range of ≈ 20 MPa$\sqrt{\text{m}}$ to ≈ 40 MPa$\sqrt{\text{m}}$, Mrówka et al. (2006), Salamci (2002), Vasudevan et al. (1989). Vasudevan et al. (1989) show values of T_R ranging from about 3 to 40 for Al–Li alloys. Thus, while we have not aimed at modeling any particular real material, our predicted fracture toughness values are a factor of about 4 above the range for aluminum alloys. On the other hand, our predicted values of the dimensionless tearing modulus, T_R, are within the (broad) experimentally observed range. Also, as in our calculations, the experiments of Lautridou and Pineau (1981) on ductile steels exhibit the decrease of a quantity proportional to T_R with an increase in the number of void nucleating sites. In addition, the general features of the computed fracture surface roughness, such as the value of β and the deviation from Gaussian statistics via power law fat tails, are consistent with those seen in the experiments on an aluminum alloy reported by Ponson et al. (2006) and Vernède et al. (submitted for publication).

We have presented our results in a non-dimensional form, as appropriate for quasi-static analyses. Also, the material response is taken to be rate dependent. Hence, the results of the dynamic analyses presented may depend on loading rate either through the effect of material inertia or the effect of material rate sensitivity. The results in Fig. 4 for the crack opening displacement versus J curve indicate that neither inertia nor material rate sensitivity play a significant role prior to the onset of crack growth. However, this is not necessarily the case during crack growth. The imposed non-dimensional loading rate of $\dot{K}_I/(\dot{\varepsilon}_0 \sigma_0 \sqrt{e_x}) = 1359.4$ corresponds to $\dot{K}_I \approx 4 \times 10^6$ MPa $\sqrt{\text{m}}$/s. This rather high loading rate was chosen to reduce the computational time. Determining the roles of inertia and rate sensitivity on the ductile fracture toughness and fracture surface roughness predictions requires a parameter study that considers a broad range of loading rates.[1]

Although the material response is taken to be temperature dependent, see Eq. (9), thermal softening does not play a significant role in the calculations here. The largest temperature increase seen was of the order of 100 K, which corresponds to a decrease in flow strength of $\approx 10\%$, and occurred within localization bands having a relatively large void volume fraction and so near final failure. Also, a calculation was carried out with $\chi = 0.01$ in Eq. (8) and, compared with the corresponding case with $\chi = 0.9$, the values of J as a function of crack length differed by less than 5%, the tearing modulus T_R differed by less than 2% and the roughness $\Delta h(\delta x)$ was essentially unaffected.

The results of Tvergaard and Hutchinson (2002) provide a nice framework for interpreting our calculations. For small inclusion volume fractions, crack initiation and growth are dominated by a void-by-void process. For void-by-void

[1] Such a study is underway.

dominated crack growth processes in a J_2-flow theory solid, Rice and Johnson (1970) and Aravas and McMeeking (1985) have shown that the work of crack growth initiation is directly proportional to the spacing between voids ahead of the crack tip. Hence, the mean spacing between void nucleation sites is the key length scale. When the volume fraction of discretely modeled inclusions is small so there are relatively few such void nucleation sites, both the crack growth resistance and statistical variations are large. On the other hand, when crack initiation and growth is dominated by multiple void interactions, the spacing between void nucleation sites is not so important (as there are many of them) and statistical variations are small.

For small inclusion volume fractions, $n \le 0.071$, both J_{IC} and T_R decrease rapidly with increasing n (by a factor of 2–3 between $n=0.012$ and $n=0.071$). For larger values of n, $0.095 \le n \le 0.19$, J_{IC} and T_R are essentially independent of inclusion volume fraction n. For the full range of inclusion volume fractions considered, the mean values of J_{IC}, normalized by a fixed length, and T_R were linearly related with a larger value of J_{IC} corresponding to a larger T_R. When J_{IC} is normalized by a microstructural length, the mean inclusion spacing, the linear relation between the normalized value of J_{IC} and T_R only holds in the void-by-void dominated crack growth regime. In our calculations the material and fracture properties as well as the fracture mechanism (progressive cavitation) are fixed. The relative independence of J_{IC} and T_R of inclusion volume fraction, for $n > 0.095$ (equivalently $\ell_0 < 5.3e_x$), suggests that once there are sufficient void nucleating sites in the crack tip vicinity, the crack growth resistance is nucleation dominated, so that the processes of void growth and coalescence do not contribute much to the toughness. In this regime, the mean inclusion spacing does not provide the dominant length scale. Also, since a relatively large number of void nucleating sites are activated, there is little dependence on the specific realization for a given inclusion volume fraction.

The correlation function, $\Delta h(\delta x)$, characterizing the fracture surface roughness in the crack growth direction exhibits power law scaling, $\Delta h(\delta x) \propto \delta x^{\beta}$, for $\delta x < \xi$ while for $\delta x > \xi$, the value of $\Delta h(\delta x)$ gradually tends towards a saturation value, Δh_s, Fig. 9. By way of contrast, the Hurst exponent β extracted from the self-affine region of the correlation function is $\beta = 0.53$ with a standard error of 0.0023 for the full range of inclusion volume fractions analyzed.

The value of the roughness exponent (or the fractal dimension) is sensitive to the roughness analysis procedure, in calculations as well as in experiments (Charkaluk et al., 1998), and to the range of power law fit to the correlation function. We note that Ponson et al. (2013) investigated the effect of varying fracture properties for a fixed inclusion distribution on fracture surface roughness and, using an analysis procedure like the one used here, found nearly the same value of β as obtained in the present calculations. That β is independent of inclusion spacing and fracture properties can be rationalized by noting that the roughness in a random microstructure is close to a random walk (for which $\beta = 0.5$) but biased to a larger value of β by the tendency of cracks (and micro-cracks) to continue growing, at least for a while, in the same direction. This provides a possible explanation of why β is nearly constant for a wide range of materials and loading conditions.

Since the value of β is not sensitive to the microstructural variations considered, it is not a useful quantity for relating toughness and roughness. However, the value of the cut-off size scale for power law behavior, ξ, is linearly related to J_{IC} and T_R when the void-by-void crack growth process dominates. The corresponding roughness amplitude Δh_s (see Fig. 10) exhibits a similar variation. This indicates that, in this regime, ξ and Δh_s are related to the mean spacing of void nucleating sites in the same way as J_{IC} and T_R are. On the other hand when crack growth is dominated by the multiple void interaction process the mean inclusion spacing does not play a significant role in the fracture process and the connection between these quantities is lost. In the experiments of Hinojoso and Aldaco (2002) the cut-off length scale of the self-affine region of the fracture surface roughness was shown to correlate with the largest microstructural heterogeneity, the grain size. In the calculations of Needleman et al. (2012), ξ was found to be roughly related to the deviation of crack path from the initial crack plane. In our results ξ and Δh_s are approximately linearly correlated for $n \le 0.071$ ($\ell_0 \ge 5.83e_x$). Hence, a possible physical description of ξ is that it is related to the wave length of the larger zig-zag excursions of the crack path (the self-affine scaling of the crack path implies that zig-zags with various length scales up to size ξ are represented on the fracture surface). We found that the values of ξ and Δh_s (as defined in Fig. 9) were nearly insensitive to the details of the fracture surface roughness analysis.

As pointed out by Vernède et al. (submitted for publication) and Ponson et al. (2013) consideration of the full statistics of the fracture surface roughness provides additional information. The full statistics of the fracture surface roughness of the computed ductile fracture surfaces are not Gaussian. The deviation from Gaussian statistics is conveniently quantified in terms of Student's t-distribution, see Ponson et al. (2013), which has a power law rather than an exponential tail. This deviation implies that large height fluctuations on the fracture surfaces are not exponentially rare as is the case for brittle fracture surfaces, Ponson et al. (2007). Our results show that the parameter, ξ_2, characterizing the cross-over from power law statistics to Gaussian statistics can be related to J_{IC} and T_R, again as long as the fracture process is void-by-void dominated.

In the calculations here only one length scale has been varied, the mean inclusion spacing. The other length scales in the formulation, for example the inclusion size are kept fixed. In addition to physical length scales, another length scale is the finite element mesh spacing. It is clear that the finite element mesh spacing will dominate in two limiting cases: (i) no inclusions ($n=0$) and (ii) all material in the crack tip vicinity is an inclusion ($n=1$). We cannot guarantee that the finite element length scale does not play a role but the strong dependence of fracture toughness and roughness parameters on inclusion volume fraction in the range $0.012 \le n \le 0.071$ suggests that in this range the finite element mesh spacing does not significantly affect at the least the qualitative response.

Our analyses pertain to a specific fracture mechanism, void nucleation and growth from a random distribution of inclusions that nucleate voids at a relatively small strain and link up via progressive cavitation initiated at uniformly distributed particles.

This has enabled us to isolate the effects of a single microstructural feature, the volume fraction (or mean spacing) of inclusions. For real materials, of course, the fracture processes can be more complex. For example, the relation between J_{IC} and T_R may depend on material and fracture properties, the active fracture mechanisms and microstructural length scales as discussed by Ritchie and Thompson (1985). Also, cleavage can occur in ligaments with a sufficiently high stress. Even restricting attention to porosity induced crack growth, the fracture process in polycrystalline structural metals can be dominated by voids that nucleate and grow along grain boundaries. Such processes will affect both the fracture toughness and the fracture surface roughness. The framework here can be extended to incorporate such effects as well as to investigate variations in constitutive properties and variations in loading mode and rate.

7. Conclusions

We have analyzed a mode I small scale yielding for a model 3D microstructure for which crack growth occurs by the nucleation, growth and coalescence of voids originating from: (i) larger inclusions that nucleate voids relatively early in the deformation history and (ii) smaller particles that nucleate voids at much larger strains. The fixed size larger inclusions are modeled discretely with all other material and fracture properties fixed. Our analyses have quantified fracture toughness and the statistics of fracture surface roughness for eight volume fractions of inclusions and, for each inclusion volume fraction, seven random distributions (five for the smallest inclusion volume fraction). For a sufficiently small volume fraction of inclusions, the mean spacing between the larger inclusions serves as a characteristic length.

1. Two regimes of crack growth behavior occur. For small inclusion volume fractions (≤ 0.071 for the parameters here) crack growth is dominated by a void-by-void process and the mean spacing between inclusions serves as a characteristic length. For larger inclusion volume fractions, crack growth involves multiple void interactions and the mean inclusion spacing is not the dominant length scale.
2. For small inclusion volume fractions (the void-by-void dominated crack growth regime), the values of J_{IC} and the tearing modulus T_R decrease rapidly with increasing inclusion volume fraction (decreasing mean spacing). For larger inclusion volume fractions (the multiple void interaction regime), the values of J_{IC} and the tearing modulus T_R show little or no dependence on inclusion volume fraction.
3. Regardless of whether J_{IC} is normalized by a fixed length for all inclusion volume fractions or by the mean inclusion spacing, a linear relation between the normalized value of J_{IC} and T_R is found for small inclusion volume fractions (the void-by-void dominated crack growth regime).
4. For the full range of inclusion volume fractions considered, the computed fracture surfaces are self-affine over a size range of nearly two orders of magnitude with the surface roughness correlation function exhibiting power law behavior with a Hurst exponent ≈ 0.53.
5. The computed fracture surface roughness distributions are not Gaussian but they are well fit by Student's t-distribution. Parameters characterizing the Student's t-distribution fit depend on the inclusion volume fraction.
6. Parameters characterizing the fracture surface roughness, such as the cut-off length, ξ, the saturation value of the correlation function, Δh_s, and cross-over length, ξ_2, are linearly related to J_{IC} and the tearing modulus T_R for small inclusion volume fractions which is the regime in which crack growth occurs by a void-by-void process but no such relation is found for larger inclusion volume fractions which is when crack growth involves multiple void interactions.

Acknowledgments

The financial support provided by the U.S. National Science Foundation, Grant CMMI-1200203 (AS, SO, AN), and by the European Union, ToughBridge Marie Curie Grant (LP), is gratefully acknowledged. Dr. Stéphane Vernède is gratefully acknowledged for fruitful discussions on the roughness statistical analysis methodology. We are grateful for the insightful comments provided by Professors J.R. Rice of Harvard University and K. Ravi-Chandar of the University of Texas at Austin, and also for the constructive criticisms and suggestions of an anonymous reviewer.

References

Afek, I., Bouchbinder, E., Katzav, E., Mathiesen, J., Procaccia, I., 2005. Void formation and roughening in slow fracture. Phys. Rev. E 71, 066127.
Aravas, N., McMeeking, R.M., 1985. Finite element analysis of void growth near a blunting crack tip. J. Mech. Phys. Solids 33, 25–49.
ASM Handbook, 1987. Fractography, vol. 12, ASM International.
ASTM E1820-11, 2011. Standard test method for measurement of fracture toughness, ASTM International.
Barabasi, A.-L., Stanley, H.E., 1995. Fractal Concepts in Surface Growth. Cambridge University Press, Cambridge, England.
Becker, R., Needleman, A., Suresh, S., Tvergaard, V., Vasudevan, A.K., 1989. An analysis of ductile failure by grain boundary void growth. Acta Metall. 37, 99–120.
Belytschko, T., Chiapetta, R.L., Bartel, H.D., 1976. Efficient large scale non-linear transient analysis by finite elements. Int. J. Numer. Methods Eng. 10, 579–596.
Benzerga, A.A., Leblond, J.B., 2010. Ductile fracture by void growth to coalescence. Adv. Appl. Mech. 44, 169–305.
Bonamy, D., Bouchaud, E., 2011. Failure of heterogeneous materials: a dynamic phase transition? Phys. Rep. 498, 1–44.

Bonamy, D., Ponson, L., Bouchaud, E., Prades, S., Guillot, C., 2006. Scaling exponents for fracture surfaces in homogeneous glass and glassy ceramics. Phys. Rev. Lett. 97, 135504.
Bouchaud, E., Lapasset, G., Planes, J., 1990. Fractal dimension of fractured surfaces: a universal value?. Europhys. Lett. 13, 73–79.
Bouchaud, E., 1997. Scaling properties of cracks. J. Phys. Condensed Matter 9, 4319–4344.
Bouchbinder, E., Mathiesen, J., Procaccia, I., 2004. Roughening of fracture surfaces: the role of plastic deformation. Phys. Rev. Lett. 92, 245505.
Bouchbinder, E., Procaccia, I., Santucci, S., Vanel, L., 2006. Fracture surfaces as multiscaling graphs. Phys. Rev. Lett. 96, 055509.
Carney, L.R., Mecholsky Jr., J.J., 2013. Relationship between fracture toughness and fracture surface fractal dimension in AISI 4340 steel. Mater. Sci. Appl. 4, 258–267.
Charkaluk, E., Bigerelle, M., Iost, A., 1998. Fractals and fracture. Eng. Fract. Mech. 61, 119–139.
Cherepanov, G.P., Balankin, A.S., Ivanova, V.S., 1995. Fractal fracture mechanics—a review. Eng. Fract. Mech. 51, 997–1033.
Chu, C.C., Needleman, A., 1980. Void nucleation effects in biaxially stretched sheets. J. Eng. Mater. Technol. 102, 249–256.
Dauskardt, R.H., Haubensak, F., Ritchie, R.O., 1990. On the interpretation of the fractal character of fracture surfaces. Acta Metall. Mater. 38, 143–159.
Davidson, D.L., 1989. Fracture surface roughness as a gauge of fracture toughness: aluminium-particulate SiC composites. J. Mater. Sci. 24, 681–687.
Feder, J., 1988. Fractals. Plenum Press, New York.
Garrison Jr., W.M., Moody, N.R., 1987. Ductile fracture. J. Phys. Chem. Solids 48, 1035–1074.
Goods, S.H., Brown, L.M., 1979. The nucleation of cavities by plastic deformation. Acta Metall. 27, 1–15.
Gurland, J., Plateau, J., 1963. The mechanism of ductile rupture of metals containing inclusions. Trans. ASM 56, 442–454.
Gurson, A.L., 1975. Plastic Flow and Fracture Behavior of Ductile Materials Incorporating Void Nucleation, Growth and Interaction (Ph.D. thesis), Brown University, Providence, RI.
Hinojoso, M., Aldaco, J., 2002. Self-affine fracture surface parameters and their relationship with microstructure in a cast aluminum alloy. J. Mater. Res. 17, 1276–1282.
Lautridou, J.C., Pineau, A., 1981. Crack initiation and stable crack growth resistance in A508 steels in relation to inclusion distribution. Eng. Fract. Mech. 15, 55–71.
Mandelbrot, B.B., 1983. The Fractal Geometry of Nature. W.H. Freeman, New York, NY.
Mandelbrot, B.B., Passoja, D.E., Paullay, A.J., 1984. Fractal character of fracture surfaces of metals. Nature 308, 721–722.
Mandelbrot, B.B., 1985. Self-affine fractals and fractal dimension. Phys. Scr. 32, 257–260.
Mathur, K.K., Needleman, A., Tvergaard, V., 1996. Three dimensional analysis of dynamic ductile crack growth in a thin plate. J. Mech. Phys. Solids 44, 439–464.
McClintock, F.A., 1968. A criterion for ductile fracture by the growth of holes. J. Appl. Mech. 35, 363–371.
Moreira, J.G., da Silva, J.K.L., Kamphorst, S.O., 1994. On the fractal dimension of self-affine profiles. J. Phys. A 27, 8079–8089.
Mrówka, G., Sieniawski, J., Nowotnik, A., 2006. Tensile properties and fracture toughness of heat treated 6082 alloy. J. Achiev. Mater. Manuf. Eng. 17, 105–108.
Mu, Z.K., Lung, C.W., 1988. Studies on the fractal dimension and fracture toughness of steel. J. Phys. D Appl. Phys. 21, 848–850.
Needleman, A., Tvergaard, V., 1987. An analysis of ductile rupture modes at a crack tip. J. Mech. Phys. Solids 35, 151–183.
Needleman, A., Tvergaard, V., Bouchaud, E., 2012. Prediction of ductile fracture surface roughness scaling. J. Appl. Mech. 79, 031015.
Pan, J., Saje, M., Needleman, A., 1983. Localization of deformation in rate sensitive porous plastic solids. Int. J. Fract. 21, 261–278.
Pande, C.S., Richards, L.E., Louat, N., Dempsey, B.D., Schwoeble, A.J., 1987. Fractal characterization of fractured surfaces. Acta Metall. 35, 1633–1637.
Paris, P.C., Tada, H., Zahoor, A., Ernst, H., 1979. The theory of instability of the tearing modes in elastic-plastic crack growth. In: Landes, J.D., Begley, J.A., Clarke, G.A. (Eds.), Elastic-Plastic Fracture, ASTM STP 668, American Society for Testing and Materials, pp. 5–36.
Peirce, D., Shih, C.F., Needleman, A., 1984. A tangent modulus method for rate dependent solids. Comput. Struct. 18, 875–887.
Ponson, L., Bonamy, D., Bouchaud, E., 2006. Two-dimensional scaling properties of experimental fracture surfaces. Phys. Rev. Lett. 96, 035506.
Ponson, L., Auradou, H., Pessel, M., Lazarus, V., Hulin, J-P., 2007. Failure mechanisms and surface roughness statistics of fractured Fontainebleau sandstone. Phys. Rev. E 76, 036108.
Ponson, L., Cao, Y., Bouchaud, E., Tvergaard, V., Needleman, A., 2013. Statistics of ductile fracture surfaces: the effect of material parameters. Int. J. Fract. http://dx.doi.org/10.1007/s10704-013-9846-z.
Ponson, L., Srivastava, A., Osovski, S., Bouchaud, E., Tvergaard, V., Needleman, A. Correlating toughness and roughness in ductile fracture, submitted for publication.
Puttick, K.E., 1959. Ductile fracture in metals. Philos. Mag. 4, 964–969.
Ramanathan, S., Ertas, D., Fisher, D.S., 1997. Quasistatic crack propagation in heterogeneous media. Phys. Rev. Lett. 79, 873–876.
Ray, K.K., Mandal, G., 1992. Study of correlation between fractal dimension and impact energy in a high strength low alloy steel. Acta Metall. Mater. 40, 463–469.
Rice, J., 1968. A path-independent integral and the approximate analysis of strain concentration by notches and cracks. J. Appl. Mech. 35, 379–386.
Rice, J.R., Tracey, D.M., 1969. On the ductile enlargement of voids in triaxial stress fields. J. Mech. Phys. Solids 17, 201–217.
Rice, J.R., Johnson, A., 1970. The role of large crack tip geometry changes in plane strain fracture. In: Kanninen, M.F., et al. (Eds.), Inelastic Behavior of Solids. McGraw-Hill, NY, pp. 641–672.
Richards, L.E., Dempsey, B.D., 1988. Fractal characterization of fractured surfaces in Ti–4.5Al–5.0Mo–1.5Cr (CORONA 5). Scr. Metall. 22, 687–689.
Ritchie, R.O., Thompson, A.W., 1985. On macroscopic and microscopic analyses for crack initiation and crack growth toughness in ductile alloys. Metall. Trans. A 16A, 233–248.
Rogers, H.C., 1960. The tensile fracture of ductile metals. AIME Trans. 218, 498–506.
Salamci, E., 2002. Mechanical properties of spray cast 7XXX series aluminium alloys. Turk. J. Eng. Environ. Sci. 26, 345–352.
Su, H., Zhang, Y., Yan, Z., 1991. Fractal analysis of microstructures and properties in ferrite-martensite steels. Scr. Metall. Mater. 25, 651–654.
Tang, S., Kopacz, A.M., O'Keefe, S.C., Olson, G.B., Liu, W.K., 2013. Three-dimensional ductile fracture analysis with a hybrid multiresolution approach and microtomography. J. Mech. Phys. Solids 61, 2108–2124.
Tvergaard, V., 1981. Influence of voids on shear band instabilities under plane strain conditions. Int. J. Fract. 17, 389–407.
Tvergaard, V., 1982a. On localization in ductile materials containing spherical voids. Int. J. Fract. 18, 237–252.
Tvergaard, V., 1982b. Influence of void nucleation on ductile shear fracture at a free surface. J. Mech. Phys. Solids 30, 399–425.
Tvergaard, V., 1990. Material failure by void growth to coalescence. Adv. Appl. Mech. 27, 83–151.
Tvergaard, V., Hutchinson, J.W., 2002. Two mechanisms of ductile fracture: void by void growth versus multiple void interaction. Int. J. Solids Struct. 39, 3581–3597.
Tvergaard, V., Needleman, A., 1984. Analysis of the cup-cone fracture in a round tensile bar. Acta Metall. 32, 157–169.
Tvergaard, V., Needleman, A., 2006. Three dimensional microstructural effects on plain strain ductile crack growth. Int. J. Solids Struct. 43, 6165–6179.
Tippur, C.F., 1949. The fracture of metals. Metallurgia 33, 133–157.
Underwood, E.E., Banerji, K., 1986. Fractals in fractography. Mater. Sci. Eng. 80, 1–14.
Vasudevan, A.K., Doherty, R.D., Suresh, S., 1989. Fracture and fatigue characteristics in aluminum alloys. In: Vasudevan, A.K., Doherty, R.D. (Eds.), Aluminum Alloys—Contemporary Research and Applications, Treatise on Materials Science and Technology, vol. 31. Elsevier Science, Burlington, pp. 445–462.
Vernède, S., Ponson, L., Cao, Y., Bouchaud, J.P. Extreme events and non-gaussian statistics of experimental fracture surfaces, submitted for publication.
Wang, Z.G., Chen, D.L., Jiang, X.X., Ai, S.H., Shih, C.H., 1988. Relationship between fractal dimension and fatigue threshold value in dual-phase steels. Scr. Metall. 22, 827–832.